JACS
JOURNAL OF THE AMERICAN CHEMICAL SOCIETY
pubs.acs.org/JACS
Article

Functionalized Graphene via a One-Pot Reaction Enabling Exact Pore Sizes, Modifiable Pore Functionalization, and Precision Doping

Kira Coe-Sessions, Alathea E. Davies, Bhausaheb Dhokale, Michael J. Wenzel, Masoumeh Mahmoudi Gahrouei, Nikiphoros Vlastos, Jordan Klaassen, Bruce A. Parkinson, Laura de Sousa Oliveira,* and John O. Hoberg*

Cite This: https://doi.org/10.1021/jacs.4c10529
Read Online

ABSTRACT: Functionalizing graphene with exact pore size, specific functional groups, and precision doping poses many significant challenges. Current methods lack precision and produce random pore sizes, sites of attachment, and amounts of dopant, leading to compromised structural integrity and affecting graphene's applications. In this work, we report a strategy for the synthesis of functionalized graphitic materials with modifiable nanometer-sized pores via a Pictet−Spengler polymerization reaction. This one-pot, four-step synthesis uses concepts based on covalent organic frameworks (COFs) synthesis to produce crystalline two-dimensional materials that were confirmed by PXRD, TEM measurements, and DFT studies. These new materials are structurally analogous to doped graphene and graphene oxide (GO) but, unlike GO, maintain their semiconductive properties when fully functionalized.

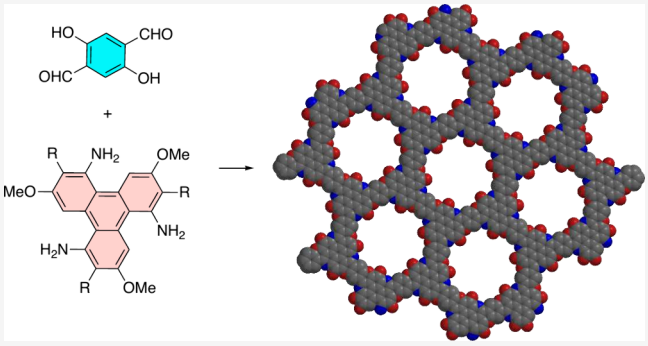

■ INTRODUCTION

Graphene, a single layer of carbon atoms arranged in a two-dimensional (2D) honeycomb lattice, has revolutionized the field of materials science with its extraordinary electrical conductivity and mechanical strength. However, the practical applications of pristine graphene have been somewhat limited due to challenges in its functionalization. Graphene oxide (GO) was developed to emulate graphene modified by introducing oxygenated functionalities into the structure via random pore formation. This modified structure incorporates hydroxyl and epoxides on the basal plane and carboxylic moieties on the sheet edges. GO does exhibit varied electrical conductivity; however, when fully functionalized it behaves as an insulator,[1,2] and in order to regain conductivity the functional groups must be chemically removed.[3−5] The elemental ratio of C:O:H in GO can vary from ∼6:2:1 to 6:4:3, and these high oxidation levels result in band gaps of ∼2−4 eV,[6] reducing conductivity. Reduced GO (rGO), produced by chemically removing the functional groups, results in band gaps below 2 eV, thus regaining conductivity. As apparent, a divergence exists between graphene, GO, and rGO involving maintaining conductivity while retaining a level of functionality. Furthermore, procedures such as ion bombardment,[7] etching,[8] or oxidation[9] produce GO with a high degree of polydispersity in both size and density of the pores.[5] When produced at high density, these randomly distributed pores start to overlap, leading to larger openings that weaken the material. It has been stated that "variations in the degree of oxidation caused by differences in starting materials (principally the graphite source) or oxidation protocol can cause substantial variation in the structure and properties of the material".[10] This lack of adaptability presents significant barriers to technological implementation and broad use. A bottom-up synthesis of a nanoporous "graphene" has been reported,[11] providing a material with ordered nanopores while maintaining the integrity of the graphene, but this nine-step synthesis provided only nanogram quantities without the flexibility of pore functionalization.

Covalent organic frameworks (COFs) are a class of crystalline materials composed of organic building blocks linked together through covalent bonds, resulting in extended periodic structures. They have emerged as a versatile class of crystalline materials[12−19] with tunable structures and functionalities, which would make the 2D versions attractive candidates as ordered alternatives to GO. Their uniqueness is their modularity that enables flexible tailoring of properties through rational design and synthesis. The quest for advanced materials

Received: August 1, 2024
Revised: September 16, 2024
Accepted: September 17, 2024

with novel electronic properties has led researchers to explore innovative material science approaches. 2D-COFs have the potential to blend the versatility of organic chemistry with the exceptional properties of graphene-related structures, and with this marriage, new possibilities for creating materials with exceptional conductivity and electrical performance, tunable band gaps, tailored porosity, and functional group modification are enabled.

Between 2010 and 2020, Wei and co-workers developed a method for the formation of triazacoronenes using a three-fold Pictet–Spengler reaction, Figure 1.[20−23] The reaction begins

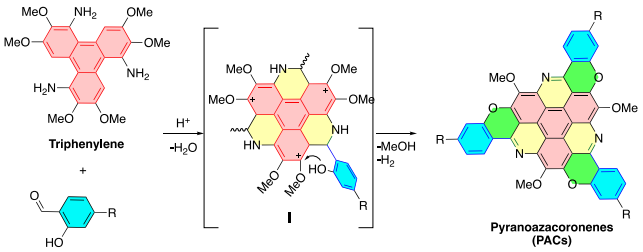

Figure 1. Pyranoazacoronene synthesis using a three-fold Pictet–Spengler reaction.

with attack of the triphenylene triamines on the aldehyde, shown in blue, to form imine linkages, followed by electrophilic aromatic cyclization to produce the new ring, shown in yellow (intermediate **I**). This intermediate cation is intercepted by the ortho hydroxyl group of the salicylaldehyde with subsequent loss of methanol to form a second ring, highlighted in green.[17,21] Dehydrogenation under an air atmosphere completes the sequence to form the aromatic pyridine ring (green bond). These pyranoazacoronenes (PACs) are 2D, highly conjugated structures generally formed in excellent yields of 80−96%. To the best of our knowledge, only one attempt at polymer formation using the triphenylene node has been attempted. In this, Coskun and co-workers used a triphenylene without methoxy groups and a non-hydroxyl dialdehyde, i.e., terephthaldehyde, to produce a nonplanar, microporous polymer.[24] However, as stated in their report, the reaction resulted in an amorphous polymer as evident from the PXRD.

In this Article, we present a new family of graphene-like 2D COFs that have a highly stable, aromatic backbone with intrinsically ordered nanometer-sized pores that can be modified with functional groups. These materials are the first PAC COFs and greatly expand the repertoire of functional graphitic materials.

■ RESULTS AND DISCUSSION

Triphenylenes are typically synthesized in three high-yielding steps from catechol derivatives via Scholl reaction[25] and nitration[26] to provide the trinitro **1**, followed by reduction (Route A) to produce **2a**, Figure 2. Synthesis of the trinitrotriphenylene **1** is easily achieved in 200 g amounts. At this stage, we developed a new triphenylene motif that involved selective demethylation of the methoxy ortho to the nitro moiety in **1**. Precedents for ortho demethylations have been reported using carbonyls as directing groups,[27] and fortunately boron tribromide was highly efficient at removing the targeted methyl group. The resulting trihydroxy **1b** can be manipulated in a variety of ways, such as reduction of the nitro groups to produce **2b**; alternatively, triflation followed by a

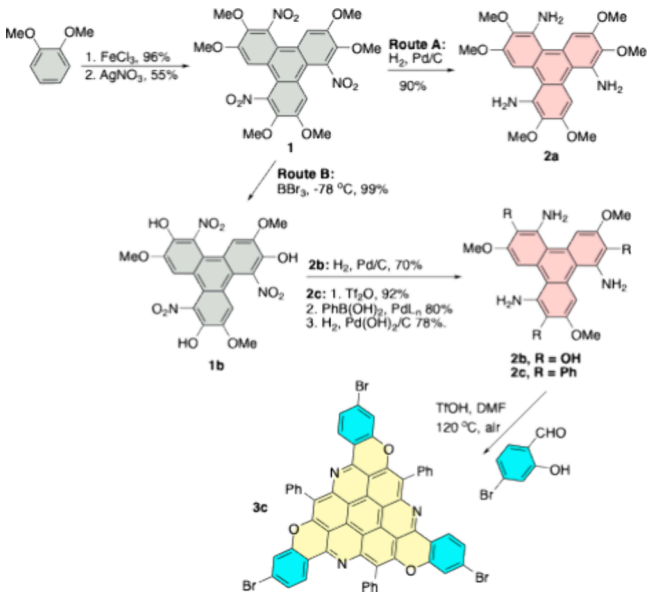

Figure 2. Synthesis of modified triphenylenes. Step 2 Suzuki coupling optimization is illustrated in SI Table 1.

carbon−carbon bond-forming Suzuki reaction with subsequent reduction gives **2c**. All are highly efficient reactions with good to excellent yields and, importantly, provide a method for pore functionalization. A successful Pictet–Spengler reaction was performed using **2c** with characterization of the resulting coronene **3c** to verify the regiochemistry of the demethylation step. Formation of **3c** requires the displacement of the MeO group in **2c**, and ^{1}H NMR and IR spectra clearly indicated the disappearance of the methoxy group and the presence of the Ph group (SI Figures S16 and S18). MALDI mass spectroscopy also firmly established **3c** with the expected isotopic distribution from the bromines (SI Figure S17).

Conditions for a COF-forming reaction were also established during the synthesis of **3c**, in which DMF and TfOH under an air atmosphere appeared to be optimal. Using these conditions, formation of COFs was next attempted and achieved by heating **2a**−**2c** with dihydroxyterephthaldehyde (TA) or with dihydroxynaphthaldehyde (NA) under the same conditions, Figure 3. It should be noted that additional conditions using NMP as a solvent, microwave heating, and inert atmosphere were investigated. However, the aforementioned conditions appeared to be optimal based on XRD and TEM analyses. These reactions produced crystalline solids that were characterized as discussed below.

Indications of successful PAC COF formation were initially established using Fourier transform infrared (FTIR) spectroscopy. In the reaction of **2a** with dihydroxyterephthaldehyde, disappearance of the amine (3395, 3320 cm^{-1}) and carbonyl (1690 cm^{-1}) stretches with the appearance of the imine stretch (1600 cm^{-1}) in COF **4a** indicated its formation (SI Figure S19). Additionally, weaker 2930 cm^{-1} C−H stretches in PAC COF **4a** further established formation. Furthermore, a comparison of the FTIR for PAC COF **4c** to that for coronene **3c** (SI Figures S56 and S16) corroborates formation, as the coronene displayed nearly identical stretches.

Powder X-ray diffraction (PXRD) was performed to evaluate the crystallinity of the materials. COF-forming reactions involving 2−3-step sequences are known,[28−44] and our sequence herein involves four sequential reactions as discussed

https://doi.org/10.1021/jacs.4c10529
J. Am. Chem. Soc. XXXX, XXX, XXX−XXX

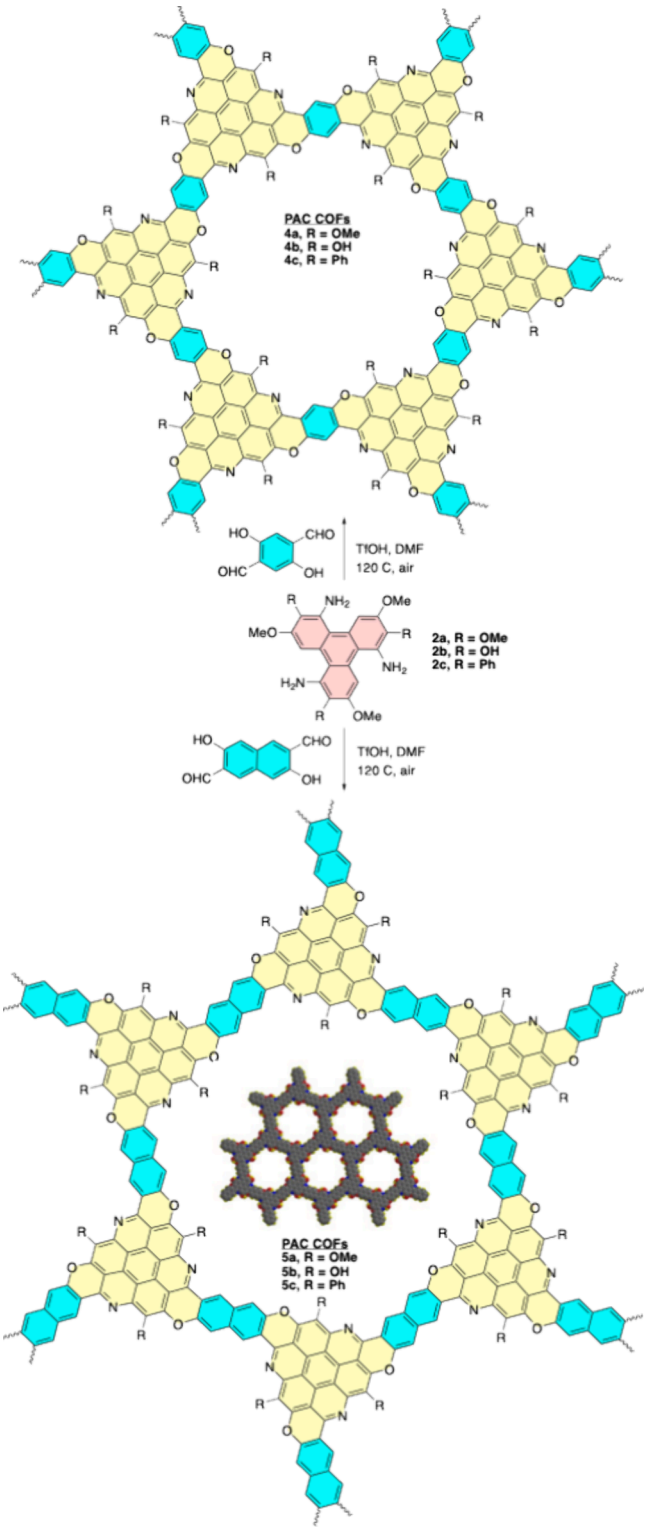

Figure 3. PAC COFs **4a**−**c** from dihydroxyterephthaldehyde (TA) and **5a**−**c** using dihydroxynaphthaldehyde (NA) with a space-filling five-pore model depicted in the NA pore.

above; reversibility in steps 2−4 is highly improbable, so a more amorphous PXRD was expected. However, the resulting PXRDs of COFs **4a** and **5a** illustrated in Figure 4 exceeded expectations. Figure 4a illustrates the PXRD of **4a** in yellow and that of **5a** in blue, with the theoretical PXRD of **5a** in black. In **4a**, peaks at 8.8°, 16.5°, and 27.3° are assignable to the 100, 200, and 002 facets, respectively. For comparison, pristine graphite exhibits a sharp 002 interlayer spacing peak at 2θ = 26.4° corresponding to a d spacing of 3.37 Å (see SI Figure S67 for PXRDs of graphite, GO, and rGO). Upon oxidation of graphite and then chemical removal of the function groups to produce rGO, a peak centered around 2θ = 26.4° reappears that is very broad, with a range >10. Thus, to claim formation of a graphitic material, an interlayer spacing must be evident, and in all our materials this is readily apparent. Furthermore, distinct from GO or rGO, the pore spacing is also evident in our materials. Thus, for the first time, graphitic materials have been synthesized demonstrating both ordered pores and layer spacing in the PXRD. Although these new COFs do not display an 002 peak equal to that of pristine graphite, they are significantly better compared to many GO, rGO, and nitrogen-doped samples (SI Figure S67). High-resolution transmission electron microscopy (HRTEM), Figure 4c−e, displayed outstanding order for COF **4a** and with all the other COFs (see SI Figures). The as-synthesized COFs displayed crystalline hexagonal structures with noticeable lattice fringes in agreement with simulated stacking motifs. For example, simulated single-area electron diffraction images of **4a** (SI Figure S88) gave excellent agreement with the TEM patterns and measurement of AB staggered in SI Figures S25 and S28. The distance across the largest hexagon in Figure 4e (0.6 Å) matches exactly with the largest hexagonal distance in the simulated ABC-stacked **4a** (SI Figure S88c). The smaller inner hexagons in the experimental diffraction (1.3−2 Å) also agree with measurements from both simulated ABD and AB staggered stacking (SI Figure S88a). Measurements from all simulated SAED images are included in the associated captions in the SI.

The stacking details were calculated with density functional theory (DFT) calculations with the Vienna Ab Initio Simulation Package (VASP) using the generalized gradient approximation (GGA) Perdew−Burke−Ernzerhof (PBE) functional (see SI for additional details and methods used). Theoretical structural simulations of COF **4a** (black in Figure 4a) confirmed an AB stacking mode with a unit cell of $a = b =$ 26 Å, c = 15 Å (α = 36°, β = 153°, γ = 120°). Lattice parameters for all modeled structures are included in the SI. In most cases, the XRD of the COFs illustrated good agreement with an AB stacking mode (see SI for the remainder), and in the case of **5c** (R = Ph) an additional peak at 11.3° was present (SI Figure S64). Good crystallinity appears to be present, with an interlayer spacing of 3.3 Å based on the peak at 2θ = 27.3°, in near perfect agreement with the theoretical layer spacing for the AB-stacked **5c** geometry (3.19 Å). Excellent agreement in **5a** between experiment and theory is also observed for the peaks at 2θ = 6.3°, 14.0°, and 26.2°. Moreover, matching peaks in the 45° range are also observed, and, importantly, a clear shift for the pore size is observed between **5a** and **4a**. In instances where comparison of XRD patterns did not provide absolute clarity on the stacking configuration, additional stacking motifs were modeled (see SI Figures S87−S92), and SAED images were generated with the software CrystalMaker[45] and SingleCrystal. For these COFs—**4a**, **4b**, and **5b**—the XRD indicated random stacking configurations for long-range order. The modeled SAED patterns, when compared to the experimental TEM diffraction, point toward localized AB or ABC stacking, resulting in clear hexagonal patterns. Greater linker lengths and smaller R group sizes lead to increased waviness in the 2D-COF geometries, as illustrated

https://doi.org/10.1021/jacs.4c10529
J. Am. Chem. Soc. XXXX, XXX, XXX−XXX

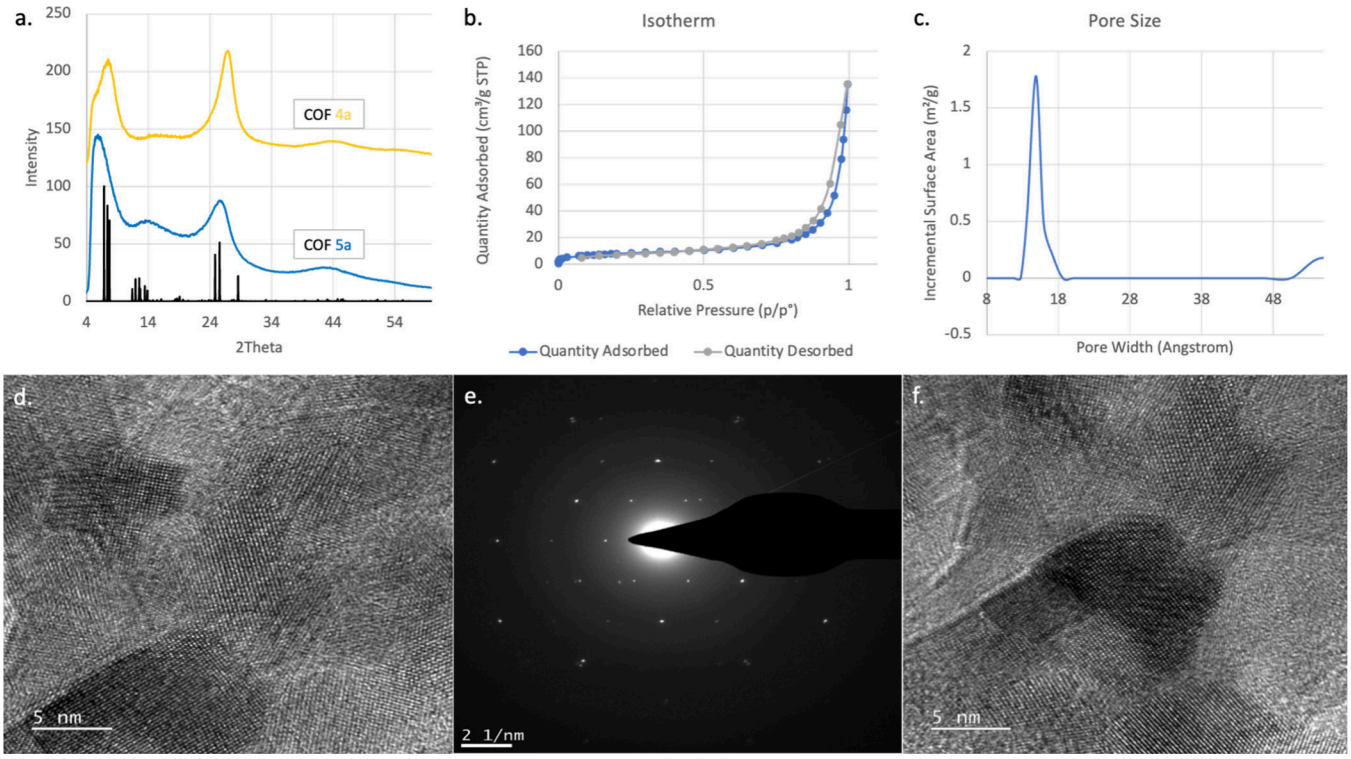

Figure 4. (a) PXRD of COFs **4a** (yellow) and **5a** (blue), with theoretical PXRD of **5a** in black. (b, c) COF **4a** N_2 sorption and PSD curves. (d, f) TEM images of COF **4a**, with diffraction pattern in (e) from panel d.

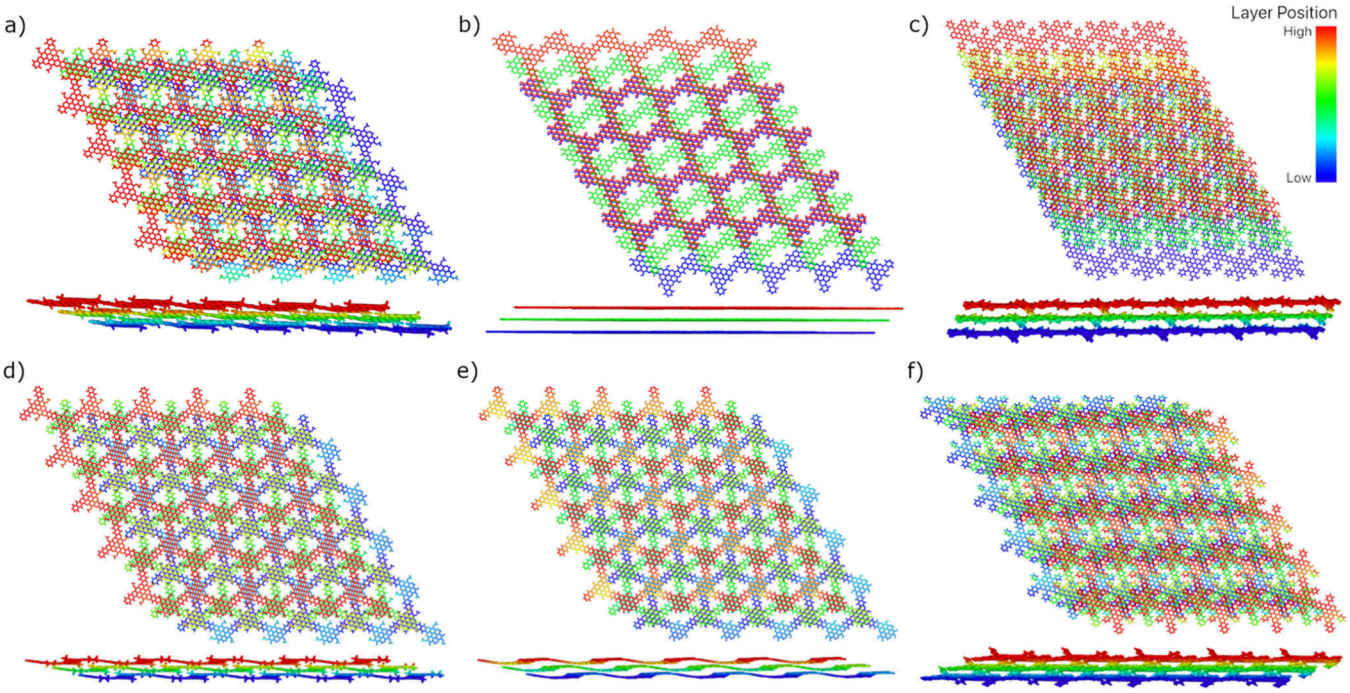

Figure 5. AB stacking of all modeled PACs COFs: (a) **4a**, (b) **4b**, (c) **4c**, (d) **5a**, (e) **5b**, and (f) **5c**. Images show both top-down and side views for each COF. The structures have been colored to show variations in height, where red indicates higher positions and blue indicates lower positions.

in Figure 5. The layers of COF **4a** (Figure 5a) are relatively planar, while in **5a** (Figure 5d) they become wavy. The length of the naphthalene linker and the small size of the methoxy R group allow the PACs' nodes over a pore to sink down closer to the node in the alternating layer. This feature is also seen in **4b** and **5b** (Figure 5b and e, respectively). This is also evident in the top-down images, where the topmost layer color fluctuates from red to yellow as the node rises above the node stacked below (red) and sinks into the pore below (yellow). COFs **4c** and **5c** (Figure 5c and f), however, are relatively planar, regardless of the length of the linker. This can be attributed to the phenyl R groups being too bulky in size to allow the PACs' nodes to sink into the pore. The waviness of **5a** and **5b** results in a changing interlayer spacing that

https://doi.org/10.1021/jacs.4c10529
J. Am. Chem. Soc. XXXX, XXX, XXX−XXX

corresponds to broader peaks in the experimental XRDs. Finally, a zoomed-out view of the theoretically predicted geometry for **4a** (SI Figure S82) illustrates how the lattice fringes and hexagonal diffraction pattern emerge in the AB-stacked framework.

Surface area and porosity were calculated with Zeo++[46] for each of the modeled geometries (SI Table S4). Nitrogen adsorption isotherms (BET), Figure 4b,c, confirmed a pore spacing of 14.8 Å for **4a**, which is in agreement with the calculated distance between methyl groups of 14.4 Å. The experimental PXRD is in good agreement with the theoretical AB-stacked optimized geometry. This, in turn, suggests that BET is only measuring the surface area at the surface of the stacked COF flakes and/or that some AA-stacking character is present in **4a**, given that nitrogen could not penetrate the bulk of the material for any of the AB-stacked PAC COFs (SI Table S4) due to a predicted pore-limiting diameter that is smaller than the kinetic diameter of nitrogen. The .vasp files for all modeled geometries and stacking, example INCAR and KPOINTS files, and a bash script for running Zeo++ have all been uploaded to a Zenodo data set (see Data Availability statement).

The importance of thermal stability for semiconducting applications significantly influences the reliability, longevity, performance, and efficiency over time due to derating. DSC-TGA revealed the remarkable stability of these materials. For example, **4a** showed a small water loss of ∼10% (SI Figure S23), followed by only small weight loss up to 800 °C, in which 60% of the material was still intact. COFs **5a** (SI Figure S36) and **5c** (SI Figure S65) were also analyzed and were equally stable.

As discussed in the Introduction, graphene is converted to GO to tune the electrical, thermal, and physical properties via pore functionality, increasing its usefulness in a variety of applications. At issue, though, is that highly oxidized GO's electrical conductivity drastically decreases, resulting in an insulating material, and regaining semiconducting properties requires a near complete removal of functional groups.[47] Testing of the semiconductor properties of these PAC COFs for comparison to those of GO was therefore undertaken. Two-point measurements were employed to determine carrier mobility and the temperature dependence of conductivity (see SI for procedures). The results in Table 1 illustrate the profound advantage these PAC COFs have over GO. With sp^3-hybridized functional groups in the pores (rows 2−5), the materials display semiconducting properties, with band gap values in the 1.0−1.3 eV range, while functionalization with phenyl groups increased the band gaps and decreases conductivity (rows 6 and 7). Additionally, comparison of the TA vs the NA systems (rows 2 vs 3 and 4 vs 5) illustrates how increasing the conjugation lowers the band gap. The phenyl group within the pore also has a noticeable effect and could be changing conduction in a variety of ways: decreasing mobility from flake to flake, decreasing flake size, increasing defects, or even acting to localize electrons.

Table 1. Band Gaps and Electrical Conductivities σ at 300 K for COFs 4 and 5

	COF	Band Gap (eV)		σ (S m^{-1})	
		Exp	Theor	Exp	Theor
2	TA OMe (**4a**)	1.3	1.03	1.2×10^{-10}	1.8×10^{4}
3	NA OMe (**5a**)	1.0	1.08	3.9×10^{-10}	2.1×10^{4}
4	TA OH (**4b**)	1.3	0.98	2.5×10^{-10}	2.3×10^{4}
5	NA OH (**5b**)	1.0	0.96	2.7×10^{-10}	1.4×10^{4}
6	TA Ph (**4c**)	1.9	1.26	6.7×10^{-12}	8.3×10^{3}
7	NA Ph (**5c**)	1.9	1.3	2.9×10^{-12}	1.9×10^{4}

The computational results corroborate the experimental findings. It is widely known that DFT calculations, particularly those performed without hybrid functionals, tend to underestimate the value of the band gap. Therefore, focus was placed on the relative changes and trends in the band gap across structures. It is expected that the presence of oxygen lone pairs in the methoxy- and hydroxy-functionalized COFs raises the energy levels of the valence bands and narrows the band gap. This can be seen in the projected density of states (PDOS) (see SI Figure S83), where there is a noticeable contribution from the O_p orbitals in the hydroxy and methoxy compared to the phenyl PAC COFs. Moreover, delocalized electrons in the phenyl COFs can move either around the backbone of the framework (longer pathway) or over the phenyl group (shorter pathway). Electrons in the phenyl groups are effectively localized, resulting in flat in-plane (Γ-K-M-Γ) valence bands and a larger band gap. The seeming disparity of the bang gap trends between TA and NA systems, which are found to be higher (identical) experimentally (theoretically), is easily resolved by inspecting the COF band structures (SI Figure S85). The band gap, obtained from the density of states calculations, is narrowed in the TA COFs in the out-of-plane region; however, conduction occurs largely in-plane (Γ-K-M-Γ), where the band gap decreases in NA, compared to that in TA for the methoxy and hydroxy COFs, as expected.

Electrical conductivity and charge mobility (SI) were calculated with BoltzTraP2[48] using the constant relaxation time approximation. Computational and measured electrical conductivity, σ, values are included in Table 1. We again find that the theoretical calculations agree with the observed trends. Note that whereas the measured electrical conductivity corresponds to undoped COFs (except for the presence of defects), the theoretical predictions correspond to a "best-case scenario", where doping is assumed to be optimal (i.e., effectively placing the chemical potential at the conduction band edge). For reference, undoped GO electrical conductivity measurements range between 5×10^{-6} [49] and 5×10^{-3} S m^{-1},[50] compared to nitrogen-doped GO at 63−78 S m^{-1}.[51] Theoretical calculations predict optimally doped GO electrical conductivity at 10^4 S m^{-1}.[52]

PAC COFs **4b** and **5b** are ideally structured for doping with metals, as they contain a hydroxyquinoline moiety. Hydroxyquinoline moieties form metal coordination complexes, as illustrated in orange at the top of Figure 6; thus, testing PAC COF **4b** for metal complexation was undertaken. Heating a mixture of **4b** and $CoCl_2$ in refluxing ethanol resulted in a clear color change and the formation of a reddish solid (see SI Figure S87). FTIR and PXRD characterization (Figures SI88 and SI89, respectively) of the solid indicated a new cobalt-doped material. The loss of the hydroxyl unit in **4b** was clearly noticeable in the IR, while the XRD spectrum displayed expected cobalt peaks. Comparison of the XRD of the new material to those of known cobalt nanoparticles (Figure SI90) confirmed a Co-doped PAC COF. As with the PAC COFs **4** and **5**, TEM images displayed highly ordered materials for the Co-doped **4b** (Figure SI91). While the exact nature of all the ligands on the cobalt would be speculative, it is likely that a chlorine and waters are present.[53]

https://doi.org/10.1021/jacs.4c10529
J. Am. Chem. Soc. XXXX, XXX, XXX−XXX

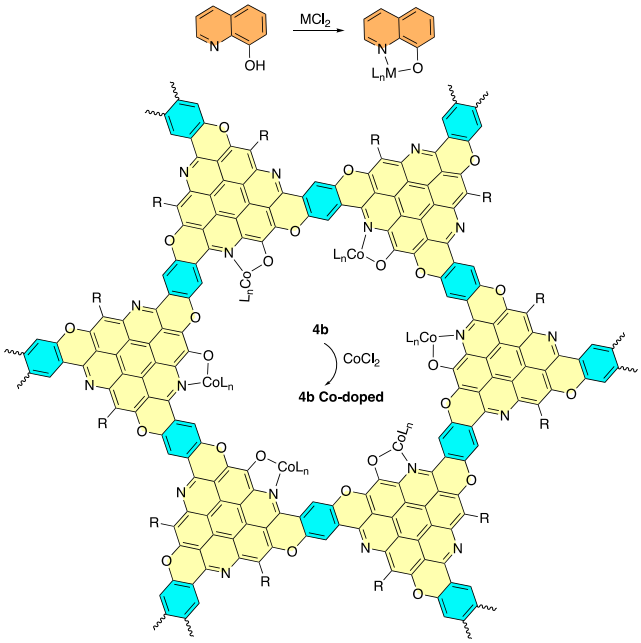

Figure 6. Formation of **4b** cobalt-doped PAC COF.

■ CONCLUSION

In summary, we designed and synthesized new, highly ordered 2D nanoporous graphene. This simple, bottom-up, one-pot reaction enables multiple pore functionalities and a multitude of pore sizes. Furthermore, the ease of reactions enables scale-up to multigram amounts, thus making it a highly practical process. Unlike GO with C:O ratios of 2:1−3:1 that produce insulating materials, these PAC COFs have a similar ratio of C:X (X = N and O) of 3.3:1 (**4b**) while still maintaining semiconducting properties. Additionally, a comparison of these PAC COFs to cobalt- and nitrogen-doped graphene illustrates a further advantage. Whereas exact placement and amounts of the nitrogen are achieved in the PAC COFs, in graphene only random numbers and placement are possible. Furthermore, we have illustrated the potential of these systems with a highly ordered metal-doped material. Future work will involve the introduction of additional metals and studies of the electronic properties they offer.

■ ASSOCIATED CONTENT

Data Availability Statement

The structure files for all modeled geometries, as well as INCAR and KPOINT files for the VASP calculations, Zeo++ input files, the raw data, and the Python script used for electronic structures analyses, are all available through Zenodo.

Supporting Information

The Supporting Information is available free of charge at https://pubs.acs.org/doi/10.1021/jacs.4c10529.

Materials and Methods, including all experimental and characterization data for the synthesis of starting monomers and COFs, including MS, NMR, IR, XRD, TEM data, and DSC-TGA (PDF)

■ AUTHOR INFORMATION

Corresponding Authors

John O. Hoberg − *Department of Chemistry, University of Wyoming, Laramie, Wyoming 82071, United States;* orcid.org/0000-0003-3833-8122; Email: hoberg@uwyo.edu

Laura de Sousa Oliveira − *Department of Chemistry, University of Wyoming, Laramie, Wyoming 82071, United States*; Email: laura.desousaoliveira@uwyo.edu

Authors

Kira Coe-Sessions − *Department of Chemistry, University of Wyoming, Laramie, Wyoming 82071, United States*

Alathea E. Davies − *Department of Chemistry, University of Wyoming, Laramie, Wyoming 82071, United States*

Bhausaheb Dhokale − *Department of Chemistry, University of Wyoming, Laramie, Wyoming 82071, United States;* orcid.org/0000-0001-7520-4727

Michael J. Wenzel − *Department of Chemistry, University of Wyoming, Laramie, Wyoming 82071, United States*

Masoumeh Mahmoudi Gahrouei − *Department of Chemistry, University of Wyoming, Laramie, Wyoming 82071, United States*

Nikiphoros Vlastos − *Department of Chemistry, University of Wyoming, Laramie, Wyoming 82071, United States*

Jordan Klaassen − *Department of Chemistry, University of Wyoming, Laramie, Wyoming 82071, United States*

Bruce A. Parkinson − *Department of Chemistry, University of Wyoming, Laramie, Wyoming 82071, United States;* orcid.org/0000-0002-8950-1922

Complete contact information is available at: https://pubs.acs.org/10.1021/jacs.4c10529

Notes

The authors declare no competing financial interest.

■ ACKNOWLEDGMENTS

The authors acknowledge financial support for this work from NSF DMREF-2118592, the UW Center of Energy Materials, and the U.S. Department of Energy, Office of Basic Energy Sciences, Division of Materials Sciences and Engineering, under Award DE-SC0024156 (standard DFT calculations). The authors would also like to acknowledge the use of computational resources at the NCAR-Wyoming Supercomputing Center provided by the National Science Foundation and the State of Wyoming, and supported by NCAR's Computational and Information Systems Laboratory (Project WYOM0145),[54] and the Advanced Research Computing Center, Beartooth Computing Environment at the University of Wyoming.[55]

■ REFERENCES

(1) Eda, G.; Mattevi, C.; Yamaguchi, H.; Kim, H.; Chhowalla, M. Insulator to Semimetal Transition in Graphene Oxide. *J. Phys. Chem. C* **2009**, *113* (35), 15768−15771.

(2) Dvorak, M.; Wu, Z. Geometrically Induced Transitions between Semimetal and Semiconductor in Graphene. *Phys. Rev. B* **2014**, *90* (11), 115415.

(3) Wu, J.; Lin, H.; Moss, D. J.; Loh, K. P.; Jia, B. Graphene Oxide for Photonics, Electronics and Optoelectronics. *Nat. Rev. Chem.* **2023**, *7* (3), 162−183.

(4) Dreyer, D. R.; Park, S.; Bielawski, C. W.; Ruoff, R. S. The Chemistry of Graphene Oxide. *Chem. Soc. Rev.* **2010**, *39* (1), 228−240.

(5) Yu, W.; Sisi, L.; Haiyan, Y.; Jie, L. Progress in the Functional Modification of Graphene/Graphene Oxide: A Review. *RSC Adv.* **2020**, *10* (26), 15328−15345.

(6) Khabibrakhmanov, A. I.; Sorokin, P. B. Electronic Properties of Graphene Oxide: Nanoroads towards Novel Applications. *Nanoscale* **2022**, *14* (11), 4131−4144.

(7) Surwade, S. P.; Smirnov, S. N.; Vlassiouk, I. V.; Unocic, R. R.; Veith, G. M.; Dai, S.; Mahurin, S. M. Water Desalination Using Nanoporous Single-Layer Graphene. *Nat. Nanotechnol.* **2015**, *10* (5), 459−464.

(8) Koenig, S. P.; Wang, L.; Pellegrino, J.; Bunch, J. S. Selective Molecular Sieving through Porous Graphene. *Nat. Nanotechnol.* **2012**, *7* (11), 728−732.

(9) Rollings, R. C.; Kuan, A. T.; Golovchenko, J. A. Ion Selectivity of Graphene Nanopores. *Nature Commun.* **2016**, *7*, 11408.

(10) Dreyer, D. R.; Park, S.; Bielawski, C. W.; Ruoff, R. S. The Chemistry of Graphene Oxide. *Chem. Soc. Rev.* **2010**, *39* (1), 228−240.

(11) Moreno, C.; Vilas-Varela, M.; Kretz, B.; Garcia-Lekue, A.; Costache, M. V.; Paradinas, M.; Panighel, M.; Ceballos, G.; Valenzuela, S. O.; Peña, D.; Mugarza, A. Bottom-up Synthesis of Multifunctional Nanoporous Graphene. *Science* **2018**, *360*, 199−203.

(12) Spaulding, V.; Zosel, K.; Duong, P. H. H.; Li-Oakey, K. D.; Parkinson, B. A.; Gomez-Gualdron, D. A.; Hoberg, J. O. A Self-Assembling, Biporous, Metal-Binding Covalent Organic Framework and Its Application for Gas Separation. *Mater. Adv.* **2021**, *2* (10), 3362−3369.

(13) Kuehl, V. A.; Yin, J.; Duong, P. H. H.; Mastorovich, B.; Newell, B.; Li-Oakey, K. D.; Parkinson, B. A.; Hoberg, J. O. A Highly Ordered Nanoporous, Two-Dimensional Covalent Organic Framework with Modifiable Pores, and Its Application in Water Purification and Ion Sieving. *J. Am. Chem. Soc.* **2018**, *140* (51), 18200−18207.

(14) Kuehl, V. A.; Wenzel, M. J.; Parkinson, B. A.; Sousa Oliveira, L. de; Hoberg, J. O. Pitfalls in the Synthesis of Polyimide-Linked Two-Dimensional Covalent Organic Frameworks. *J. Mater. Chem. A* **2021**, *9* (27), 15301−15309.

(15) Kuehl, V. A.; Duong, P. H. H.; Sadrieva, D.; Amin, S. A.; She, Y.; Li-Oakey, K. D.; Yarger, J. L.; Parkinson, B. A.; Hoberg, J. O. Synthesis, Postsynthetic Modifications, and Applications of the First Quinoxaline-Based Covalent Organic Framework. *ACS Appl. Mater. Interfaces* **2021**, *13*, 37494−37499.

(16) Duong, P. H. H.; Shin, Y. K.; Kuehl, V. A.; Afroz, M. M.; Hoberg, J. O.; Parkinson, B.; van Duin, A. C. T.; Li-Oakey, K. D. Mechanistic Study of pH Effect on Organic Solvent Nanofiltration Using Carboxylated Covalent Organic Framework as a Modeling and Experimental Platform. *Sep. Purif. Technol.* **2022**, *282*, 120028.

(17) Duong, P. H. H.; Kuehl, V. A.; Mastorovich, B.; Hoberg, J. O.; Parkinson, B. A.; Li-Oakey, K. D. Carboxyl-Functionalized Covalent Organic Framework as a Two-Dimensional Nanofiller for Mixed-Matrix Ultrafiltration Membranes. *J. Membr. Sci.* **2019**, *574*, 338−348.

(18) Duong, P. H. H.; Shin, Y. K.; Kuehl, V. A.; Afroz, M. M.; Hoberg, J. O.; Parkinson, B. A.; van Duin, A. C. T.; Li-Oakey, K. D. Molecular Interactions and Layer Stacking Dictate Covalent Organic Framework Effective Pore Size. *ACS Appl. Mater. Interfaces* **2021**, *13*, 42164−42175.

(19) Brophy, J.; Summerfield, K.; Yin, J.; Kephart, J.; Stecher, J.; Adams, J.; Yanase, T.; Brant, J.; Li-Oakey, K.; Hoberg, J.; Parkinson, B. The Influence of Disorder in the Synthesis, Characterization and Applications of a Modifiable Two-Dimensional Covalent Organic Framework. *Materials* **2021**, *14* (1), 71.

(20) Wei, J.; Han, B.; Guo, Q.; Shi, X.; Wang, W.; Wei, N. 1,5,9-Triazacoronenes: A Family of Polycyclic Heteroarenes Synthesized by a Threefold Pictet-Spengler Reaction. *Angew. Chem., Int. Ed.* **2010**, *49* (44), 8209−8213.

(21) Liu, B.; Shi, D.; Yang, Y.; Liu, D.; Li, M.; Liu, E.; Wang, X.; Zhang, Q.; Yang, M.; Li, J.; Shi, X.; Wang, W.; Wei, J. Triazacoronene Derivatives with Three *Peri* -Benzopyrano Extensions: Synthesis, Structure, and Properties: Triazacoronene Derivatives with Three *Peri* -Benzopyrano Extensions: Synthesis, Structure, and Properties. *Eur. J. Org. Chem.* **2018**, *2018* (7), 869−873.

(22) Sun, Y.; Wang, X.; Shen, G.; Yang, T.; Yang, Y.; Li, J.; Yang, M.; Sun, H.; Wei, J. A 6π Azaelectrocyclization Strategy towards the 1,5,9-Triazacoronenes. *Adv. Synth. Catal.* **2020**, *362* (8), 1651−1656.

(23) Tan, Q.; Chen, H.; Xia, H.; Liu, B.; Xu, B. Parent and Trisubstituted Triazacoronenes: Synthesis, Crystal Structure and Physicochemical Properties. *Chem. Commun.* **2016**, *52* (3), 537−540.

(24) Lee, J.; Buyukcakir, O.; Kwon, T.; Coskun, A. Energy Band-Gap Engineering of Conjugated Microporous Polymers via Acidity-Dependent in Situ Cyclization. *J. Am. Chem. Soc.* **2018**, *140* (35), 10937−10940.

(25) Naarmann, H.; Hanack, M.; Mattmer, R. A High Yield Easy Method for the Preparation of Alkoxy-Substituted Triphenylenes. *Synthesis* **1994**, *1994* (05), 477−478.

(26) Liu, B.; Shi, D.; Yang, Y.; Liu, D.; Li, M.; Liu, E.; Wang, X.; Zhang, Q.; Yang, M.; Li, J.; Shi, X.; Wang, W.; Wei, J. Triazacoronene Derivatives with Three *Peri* -Benzopyrano Extensions: Synthesis, Structure, and Properties: Triazacoronene Derivatives with Three *Peri* -Benzopyrano Extensions: Synthesis, Structure, and Properties. *Eur. J. Org. Chem.* **2018**, *2018* (7), 869−873.

(27) Dean, F. M.; Goodchild, J.; Houghton, L. E.; Martin, J. A.; Morton, R. B.; Parton, B.; Price, A. W.; Somvichien, N. Boron Trichloride as a Selective Demethylating Agent. *Tetrahedron Lett.* **1966**, *7* (35), 4153−4159.

(28) Cusin, L.; Peng, H.; Ciesielski, A.; Samorì, P. Chemical Conversion and Locking of the Imine Linkage: Enhancing the Functionality of Covalent Organic Frameworks. *Angew. Chem., Int. Ed.* **2021**, *60* (26), 14236−14250.

(29) Das, P.; Chakraborty, G.; Roeser, J.; Vogl, S.; Rabeah, J.; Thomas, A. Integrating Bifunctionality and Chemical Stability in Covalent Organic Frameworks via One-Pot Multicomponent Reactions for Solar-Driven H_2O_2 Production. *J. Am. Chem. Soc.* **2023**, *145* (5), 2975−2984.

(30) Grunenberg, L.; Savasci, G.; Terban, M. W.; Duppel, V.; Moudrakovski, I.; Etter, M.; Dinnebier, R. E.; Ochsenfeld, C.; Lotsch, B. V. Amine-Linked Covalent Organic Frameworks as a Platform for Postsynthetic Structure Interconversion and Pore-Wall Modification. *J. Am. Chem. Soc.* **2021**, *143* (9), 3430−3438.

(31) Guo, J.; Xu, Y.; Jin, S.; Chen, L.; Kaji, T.; Honsho, Y.; Addicoat, M. A.; Kim, J.; Saeki, A.; Ihee, H.; Seki, S.; Irle, S.; Hiramoto, M.; Gao, J.; Jiang, D. Conjugated Organic Framework with Three-Dimensionally Ordered Stable Structure and Delocalized π Clouds. *Nat. Commun.* **2013**, *4* (1), 2736.

(32) Haase, F.; Troschke, E.; Savasci, G.; Banerjee, T.; Duppel, V.; Dörfler, S.; Grundei, M. M. J.; Burow, A. M.; Ochsenfeld, C.; Kaskel, S.; Lotsch, B. V. Topochemical Conversion of an Imine- into a Thiazole-Linked Covalent Organic Framework Enabling Real Structure Analysis. *Nat. Commun.* **2018**, *9* (1), 2600.

(33) Li, X.; Zhang, C.; Cai, S.; Lei, X.; Altoe, V.; Hong, F.; Urban, J. J.; Ciston, J.; Chan, E. M.; Liu, Y. Facile Transformation of Imine Covalent Organic Frameworks into Ultrastable Crystalline Porous Aromatic Frameworks. *Nat. Commun.* **2018**, *9* (1), 2998.

(34) Li, X.-T.; Zou, J.; Wang, T.-H.; Ma, H.-C.; Chen, G.-J.; Dong, Y.-B. Construction of Covalent Organic Frameworks via Three-Component One-Pot Strecker and Povarov Reactions. *J. Am. Chem. Soc.* **2020**, *142* (14), 6521−6526.

(35) Liu, H.; Chu, J.; Yin, Z.; Cai, X.; Zhuang, L.; Deng, H. Covalent Organic Frameworks Linked by Amine Bonding for Concerted Electrochemical Reduction of CO2. *Chem.* **2018**, *4* (7), 1696−1709.

(36) Liu, J.; Yang, T.; Wang, Z.-P.; Wang, P.-L.; Feng, J.; Ding, S.-Y.; Wang, W. Pyrimidazole-Based Covalent Organic Frameworks: Integrating Functionality and Ultrastability via Isocyanide Chemistry. *J. Am. Chem. Soc.* **2020**, *142* (50), 20956−20961.

(37) Segura, J. L.; Mancheño, M. J.; Zamora, F. Covalent Organic Frameworks Based on Schiff-Base Chemistry: Synthesis, Properties and Potential Applications. *Chem. Soc. Rev.* **2016**, *45* (20), 5635−5671.

(38) Vitaku, E.; Gannett, C. N.; Carpenter, K. L.; Shen, L.; Abruña, H. D.; Dichtel, W. R. Phenazine-Based Covalent Organic Framework

https://doi.org/10.1021/jacs.4c10529
J. Am. Chem. Soc. XXXX, XXX, XXX−XXX

Cathode Materials with High Energy and Power Densities. *J. Am. Chem. Soc.* **2020**, *142* (1), 16−20.

(39) Waller, P. J.; AlFaraj, Y. S.; Diercks, C. S.; Jarenwattananon, N. N.; Yaghi, O. M. Conversion of Imine to Oxazole and Thiazole Linkages in Covalent Organic Frameworks. *J. Am. Chem. Soc.* **2018**, *140* (29), 9099−9103.

(40) Waller, P. J.; Lyle, S. J.; Osborn Popp, T. M.; Diercks, C. S.; Reimer, J. A.; Yaghi, O. M. Chemical Conversion of Linkages in Covalent Organic Frameworks. *J. Am. Chem. Soc.* **2016**, *138* (48), 15519−15522.

(41) Wang, K.; Jia, Z.; Bai, Y.; Wang, X.; Hodgkiss, S. E.; Chen, L.; Chong, S. Y.; Wang, X.; Yang, H.; Xu, Y.; Feng, F.; Ward, J. W.; Cooper, A. I. Synthesis of Stable Thiazole-Linked Covalent Organic Frameworks via a Multicomponent Reaction. *J. Am. Chem. Soc.* **2020**, *142* (25), 11131−11138.

(42) Wang, P.-L.; Ding, S.-Y.; Zhang, Z.-C.; Wang, Z.-P.; Wang, W. Constructing Robust Covalent Organic Frameworks via Multicomponent Reactions. *J. Am. Chem. Soc.* **2019**, *141* (45), 18004−18008.

(43) Yang, Y.; Yu, L.; Chu, T.; Niu, H.; Wang, J.; Cai, Y. Constructing Chemical Stable 4-Carboxyl-Quinoline Linked Covalent Organic Frameworks via Doebner Reaction for Nanofiltration. *Nat. Commun.* **2022**, *13* (1), 2615.

(44) Zhu, Y.; Huang, D.; Wang, W.; Liu, G.; Ding, C.; Xiang, Y. Sequential Oxidation/Cyclization of Readily Available Imine Linkages to Access Benzoxazole-Linked Covalent Organic Frameworks. *Angew. Chem., Int. Ed.* **2024**, *63* (11), No. e202319909.

(45) *CrystalMaker*, version 11.1.1; CrystalMaker Software Ltd, Oxfordshire, England, 2014.

(46) Willems, T. F.; Rycroft, C. H.; Kazi, M.; Meza, J. C.; Haranczyk, M. Algorithms and Tools for High-Throughput Geometry-Based Analysis of Crystalline Porous Materials. *Microporous Mesoporous Mater.* **2012**, *149* (1), 134−141.

(47) Sharma, N.; Tomar, S.; Shkir, M.; Kant Choubey, R.; Singh, A. Study of Optical and Electrical Properties of Graphene Oxide. *Mater. Today: Proc.* **2021**, *36*, 730−735.

(48) Madsen, G. K. H.; Carrete, J.; Verstraete, M. J. BoltzTraP2, a Program for Interpolating Band Structures and Calculating Semi-Classical Transport Coefficients. *Comput. Phys. Commun.* **2018**, *231*, 140−145.

(49) Jaafar, E.; Kashif, M.; Sahari, S. K.; Ngaini, Z. Study on Morphological, Optical and Electrical Properties of Graphene Oxide (GO) and Reduced Graphene Oxide (rGO). *MSF* **2018**, *917*, 112−116.

(50) Pereira, N. G. A.; Gonzaléz, M. E. L.; Queiroz, A. A. A. D.; Oliveira, A. F.; Tavares Wanderley Neto, E. Higher Electrical Conductivity of Functionalized Graphene Oxide Doped with Silver and Copper (II) Ions. *Energies* **2023**, *16* (20), 7019.

(51) Witjaksono, G.; Junaid, M.; Khir, M. H.; Ullah, Z.; Tansu, N.; Saheed, M. S. B. M.; Siddiqui, M. A.; Ba-Hashwan, S. S.; Algamili, A. S.; Magsi, S. A.; Aslam, M. Z.; Nawaz, R. Effect of Nitrogen Doping on the Optical Bandgap and Electrical Conductivity of Nitrogen-Doped Reduced Graphene Oxide. *Molecules* **2021**, *26* (21), 6424.

(52) Alihosseini, M.; Ghasemi, S.; Ahmadkhani, S.; Alidoosti, M.; Esfahani, D. N.; Peeters, F. M.; Neek-Amal, M. Electronic Properties of Oxidized Graphene: Effects of Strain and an Electric Field on Flat Bands and the Energy Gap. *J. Phys. Chem. Lett.* **2022**, *13* (1), 66−74.

(53) Skorokhod, L. S.; Seifullina, I. I.; Vlasenko, V. G. Products of Complex Formation in CoCl2−1-Amino-8-Hydroxynaphthalene-2,4-Disulfonic Acid-α-Hydroxy-α-Phenylacetophenone (Benzaldehyde and Its Hydroxy Derivatives) Systems. *Russ. J. Gen. Chem.* **2009**, *79* (1), 37−41.

(54) Computational and Information Systems Laboratory, Cheyenne. *HPE/SGI ICE XA System* (NCAR Community Computing); National Center of Atmospheric Research, Boulder, CO.

(55) Advanced Research Computing Center. *Beartooth Computing Environment, X86_64 Cluster*; University of Wyoming, Laramie, WY, 2023.

https://doi.org/10.1021/jacs.4c10529
J. Am. Chem. Soc. XXXX, XXX, XXX−XXX